International Journal of Heat and Mass Transfer 51 (2008) 5578–5589

Contents lists available at ScienceDirect

International Journal of Heat and Mass Transfer

journal homepage: www.elsevier.com/locate/ijhmt

A new methodology for targeting drug-aerosols in the human respiratory system

Clement Kleinstreuer [a,b,*], Zhe Zhang [a], Zheng Li [a], William L. Roberts [a], Carlye Rojas [c]

[a] Department of Mechanical and Aerospace Engineering, North Carolina State University, Raleigh, NC 27695-7910, USA
[b] Department of Biomedical Engineering, North Carolina State University, Raleigh, NC 27695-7910, USA
[c] Human Studies Division, National Health and Environmental Effects Research Laboratory, U.S. EPA, Research Triangle Park, NC 27711, USA

ARTICLE INFO

Article history:
Received 21 November 2007
Received in revised form 4 April 2008
Available online 13 June 2008

Keywords:
Drug-aerosol inhalers
Targeted drug-aerosol delivery
Methodology for smart inhaler system
Experimental verification of new methodology

ABSTRACT

Inhalation of medicine for the treatment of lung and other diseases is becoming more and more a preferred option when compared to injection or oral intake. Unfortunately, existing devices such as the popular pressurized metered dose inhalers and dry powder inhalers have rather low deposition efficiencies and their drug-aerosol deliveries are non-directional. This is acceptable when the medicine is inexpensive and does not cause systemic side effects, as it may be the case for patients with mild asthma. However, the delivery of aggressive chemicals, or expensive insulin, vaccines and genetic material embedded in porous particles or droplets requires optimal targeting of such inhaled drug-aerosols to predetermined lung areas. The new methodology introduces the idea of a controlled air-particle stream which provides maximum, patient-specific drug-aerosol deposition based on optimal particle diameter and density, inhalation waveform, and particle-release position. The efficacy of the new methodology is demonstrated with experimentally validated computer simulations of two-phase flow in a human oral airway model with two different sets of tracheobronchial airways. Physical insight to the dynamics of the controlled air-particle stream is provided as well.

1. Introduction

Targeted drug-aerosol delivery to desired lung areas required for the treatment of a specific disease is becoming more and more a treatment option, because it is fast, convenient, and with reduced topical side effects. Common oral drug delivery devices, such as pressurized-metered-dose (pMD), dry-powder (DP) and droplet-spray (DS) inhalers (see [1,2]; among others) generate rather low particle deposition efficiencies, and they are non-directional, i.e., landing sites are unpredicted. For example, Kleinstreuer et al. [3] analyzed the popular pMDI with a spacer, modified nozzle and HFA propellant. They reported that up to 46.6% of the inhaled polydisperse droplets may reach the lung, assuming a steady flow rate of Q_{in} = 30 L/min. When using CFC-driven pMDIs without spacers, 80–90% of the medicine remains in the oropharyngeal region [4,5]. In any case, while present inhalers may deliver some of the medicine to the central lung region, most treatments require a high-percentage drug-aerosol deposition at specific lung sites, such as tumors, or in desired lung regions, e.g., alveolated ducts. For example, Kleinstreuer and Zhang [6] analyzed a critical tumor size for maximum drug-aerosol deposition under various inhalation conditions. Some drugs are so aggressive and/or expensive that targeted aerosol delivery is imperative. Clearly, the development and testing of such a new generation of inhalers is a very active research area (refer to www.uspto.gov/patft/index.html).

In this paper, the underlying methodology for a future smart inhaler system (SIS) for optimal drug-aerosol delivery is presented.

2. Methods

The hypothesis that a "controlled air-particle stream", in terms of suitable, physical particle characteristics, particle release position and inhalation waveform, can transport particles from the mouth past the oropharynx, larynx and trachea as well as through the major left or right lung bifurcations has been computationally and experimentally tested. Specifically, a steady laminar isothermal inspiratory flow rate of $Q_{in} \leqslant 10$ L/min is necessary to avoid complex airflow structures which may cause randomized particle trajectories. This could be achieved by modulating a subject's actual inhalation waveform into a rectangular one, implying steady flow. Drug-aerosols have typically effective diameters of 1–20 μm, a size range which precludes Brownian motion and high impaction parameter values; hence, they tend to follow local streamlines. The determination of suitable particle release positions for optimal site-specific targeting is the most important element of the new methodology, which is achieved via "backtracking".

* Corresponding author. Address: Department of Mechanical and Aerospace Engineering and Department of Biomedical Engineering, North Carolina State University, Raleigh, NC 27695-7910, USA. Tel.: +1 919 515 5261; fax: +1 919 515 7968.
E-mail address: ck@eos.ncsu.edu (C. Kleinstreuer).

0017-9310/$ - see front matter © 2008 Elsevier Ltd. All rights reserved.
doi:10.1016/j.ijheatmasstransfer.2008.04.052

Nomenclature

C_{DP}	drag force coefficient	t	time
D	tube diameter	U	mean velocity
d_p	particle diameter	$\vec{v}$	Fluid velocity vector
$\vec{F}_D$	drag force	$\vec{v}_p$	particle velocity vector
$\vec{g}$	gravity vector		
IP	impact factor ($= Q_{in}d_p^2$)	*Greek symbols*	
m_p	particle mass	μ	fluid dynamic viscosity
Q_{in}	inspiratory flow rate	ρ	fluid density
Re_p	particle Reynolds number ($= \rho\|\vec{v}_p - \vec{v}\|d_p/\mu$)	ρ_p	particle density
St	Stokes number ($= \rho_p d_p^2 U/(9\mu D)$)		

2.1. Computational analysis

In order to simulate and analyze microparticle transport in the human respiratory system, realistic oral and lung airway models, flow domain meshes, airflow and particle trajectory equations as well as an accurate and robust equation solver had to be established. Then, a correlation between desired airway-exit locations (or required particle deposition site) of all inhaled particles and particle-release positions at the mouth inlet had to be determined.

If suitable particle characteristics and inhalation flow rates are assumed and a representative replica of the human mouth-to-trachea airway is employed [7], different particle release positions could be determined which lead to controlled concentrations at desired trachea exit locations. Laboratory studies with the same oral airway model confirmed the computer simulation results. Additional computer experiments, with Weibel Type A and realistic bifurcations attached to the oral-airway replica indicate that the new drug-aerosol targeting methodology is meritorious.

2.1.1. Computational fluid-particle dynamics model

As shown in Fig. 1, the present upper airway model consists of an oral airway replica after Chang et al. [7] with a 2 cm circular mouth inlet and either a planar symmetric triple bifurcation [8] or an asymmetric out-of-plane tracheobronchial tree as constructed by Li et al. [9] after Horsfield et al. [10], Raabe et al. [11], and Zhang and Finlay [12].

Assuming steady, laminar 3-D incompressible airflow, the describing continuity and linear momentum equations with associated boundary conditions are discussed by Zhang and Kleinstreuer [13]. For microparticles ($d_p \geqslant 1\mu m$), a Lagrangian frame of reference to compute the trajectories can be employed. In light of the relatively large particle-to-air density ratio, dilute particle suspensions, negligible Brownian motion and thermophoretic forces, drag and gravity are considered as the dominant point forces away from the walls [14]; although, gravity plays only a role at low IP-values [15], where

$$\mathrm{IP} = Q_{in}d_p^2 \tag{1}$$

Thus, the trajectory equation can be described as

$$\frac{d}{dt}(m_p\vec{v}_p) = \vec{F}_D + m_p\vec{g} \tag{2}$$

where $\vec{v}_p$ and m_p are the velocity and mass of the particle, respectively; while $\vec{F}_D$ is the drag force which for spherical particles can be expressed as

$$\vec{F}_D = \frac{1}{8}\pi\rho d_p^2 C_{Dp}(\vec{v}_p - \vec{v})|\vec{v}_p - \vec{v}| \tag{3}$$

Here, $\vec{v}$ is the air-velocity vector; d_p is the aerodynamic particle diameter; and C_{Dp} is the drag force coefficient given by

$$C_{Dp} = C_D/C_{slip} \tag{4a}$$

where

$$C_D = \begin{cases} 24(1 + 0.15Re_p^{0.687})/Re_p & \text{for } 0.0 < Re_p \leqslant 1000 \\ 0.44 & \text{for } 1000 < Re_p \end{cases} \tag{4b, c}$$

and the particle Reynolds number is

$$Re_p = \rho|\vec{v}_p - \vec{v}|d_p/\mu \tag{4d}$$

In Eq. (4a), C_{slip} is the slip correction factor [16].

2.1.2. Numerical methods

The numerical solutions of airflow and particle transport were carried out at NCSU's High Performance Computing Center (HPC) with a user-enhanced, finite-volume based program (i.e., CFX 4.4 from Ansys, Inc., Canonsburg, PA) and an off-line parallelized particle transport code "F90" [17,18]. The commercial software uses a structured, multiblock, body-fitted coordinate discretization scheme. In the present simulation, the PISO algorithm with under-relaxation was employed to solve the flow equations. All variables are located at the centroids of the control volumes. An improved Rhie–Chow interpolation method was used to obtain the velocity components and pressure on the control volume faces from those at the control volume centers. A Quadratic Upwind (QUICK) differencing scheme, which is third-order accurate in space, was employed to model the advective terms of the transport equations. The set of linearized and discretized equations for all variables were solved using the Block Stone's method. For the calculation of particle trajectories (see Eq. (2)), geometry and velocity at all control-volume vertices were first extracted from the CFX solution and written to arrays. A second-order improved Euler predictor-corrector method [17] was then used for the integration of the particle trajectory equation. In the present simulations, 2000–30,000 randomly selected, uniformly distributed particles were released at the mouth inlet and particle-number independence of the results was tested.

The mesh topology was determined by refining the mesh until grid independence of the solution of flow and mass fraction fields was achieved. The final mesh features about 420,000 and 670,000 cells for the oral airway and four-generation airway model, respectively. The solution of the flow field at each time step was assumed to be converged when the dimensionless mass residual (total mass residual)/(mass flow rate) was $<10^{-3}$. The convergence of other variables was monitored as well. The estimated maximum artificial numerical dispersion coefficient was in the order of 10^{-11} m^2/s for this study. Typical run times for the fluid flow and mass transfer simulations on eight processors with parallel algorithm were approximately 24–65 h for the oral airway model and 8 h for the four-generation model under steady inhalation condition. Utilizing

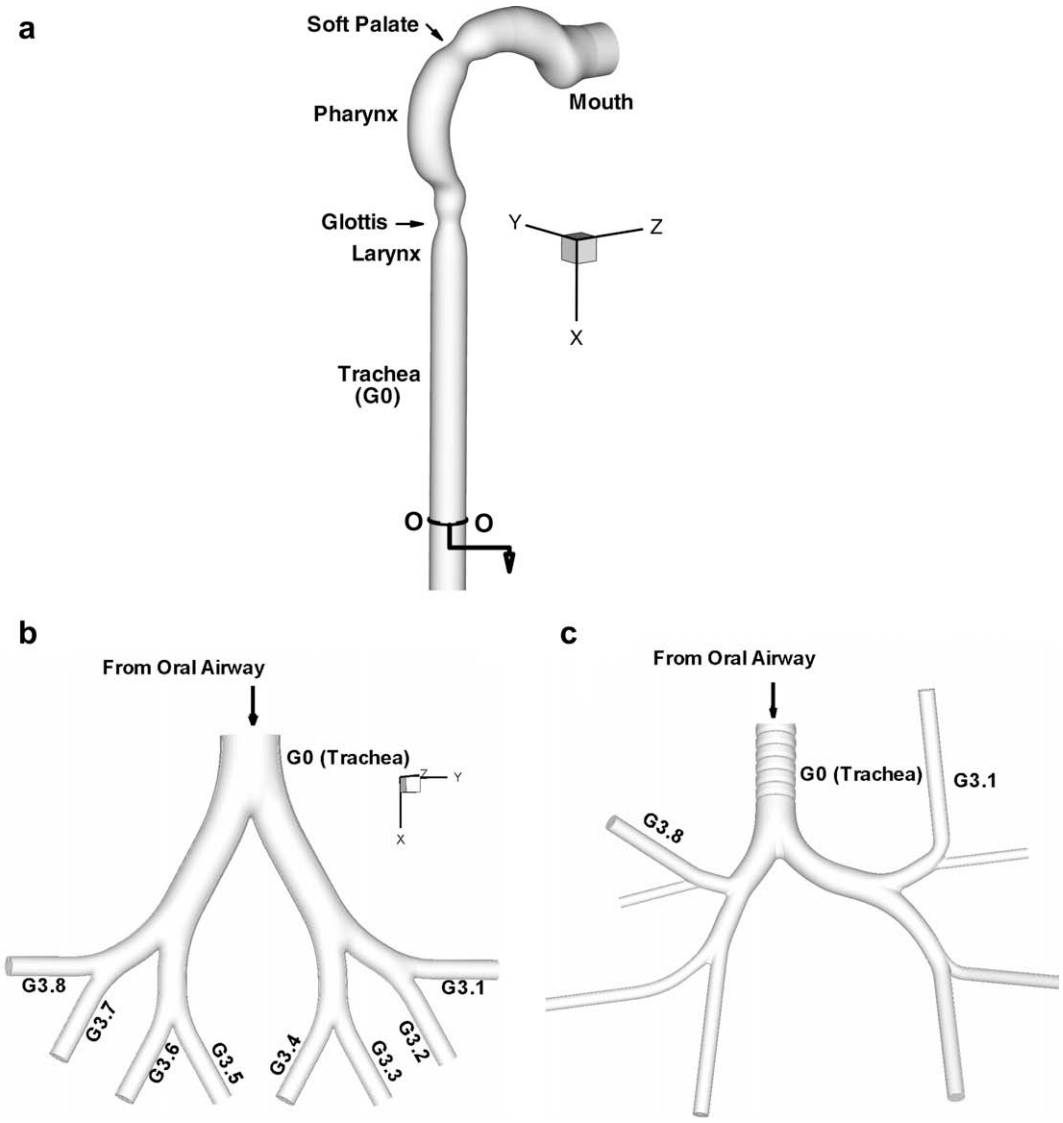

Fig. 1. 3-D views of system geometry as used for both computational and experimental models: (a) the oral airway model; (b) Weibel type A airway model; and (c) realistic tracheobronchial model (both generations G0 to G3).

the converged flow field solution, the microparticle trajectory simulations required approximately 1–5 h on four processors for each case simulated.

2.1.3. Model validations

The present computational fluid-particle dynamics (CFPD) model has been validated with various experimental data sets for steady and transient laminar flows in bifurcations [13,19–21] and for laminar, transitional and turbulent flows in tubes with local obstructions [22,23]. The accuracy of microparticle transport was evaluated in terms of simulated particle deposition fractions. For the present oral airway model, results were compared with the observations by Cheng et al. [24] for three inhalation rates (see Fig. 2a). Following Cheng et al. [24], the Stokes number is defined here as $St = \rho_p d_p^2 U/9\mu D$, with ρ_p being the particle density, d_p being the particle diameter, and U being the mean velocity evaluated as Q/A, where A is the mean cross-sectional area, and D is the minimum hydraulic diameter. A comparison of microparticle deposition in the present airway model with *in vivo* deposition data as a function of the impaction parameter is shown in Fig. 2b, where the computational data points agree well with the experimental data and nicely retrace the mean of the measured deposition data curve.

In summary, the good agreements between experimental observations and theoretical predictions instill confidence that the present computer simulation model is sufficiently accurate to analyze laminar 3-D fluid flow as well as mass transfer and particle deposition in three-dimensional oral and bifurcating airways.

2.1.4. Particle release positions

The specific mouth inlet (or inhaler outlet) positions of aerosols which exit the trachea (or any Generation 3 airway) or land on different targeted lung sites were determined via backtracking. Then, release-controlled air-particle streams were generated so that most aerosols appear at the desired exit or deposition locations. For example, Fig. 3a and b depict mouth inlet release positions of 7 μm and 20 μm particles which all reach eight outlets of Generation 3 in the symmetric bifurcation airway model (see Fig. 1) when Q_{in} = 8 L/min. Naturally, all particles released from these mouth inlet positions can bypass the oral airway and enter the bronchial airways. Clearly, the depositions of particles with d_p = 7 μm are minor in the upper airways due to relatively low inertial impaction

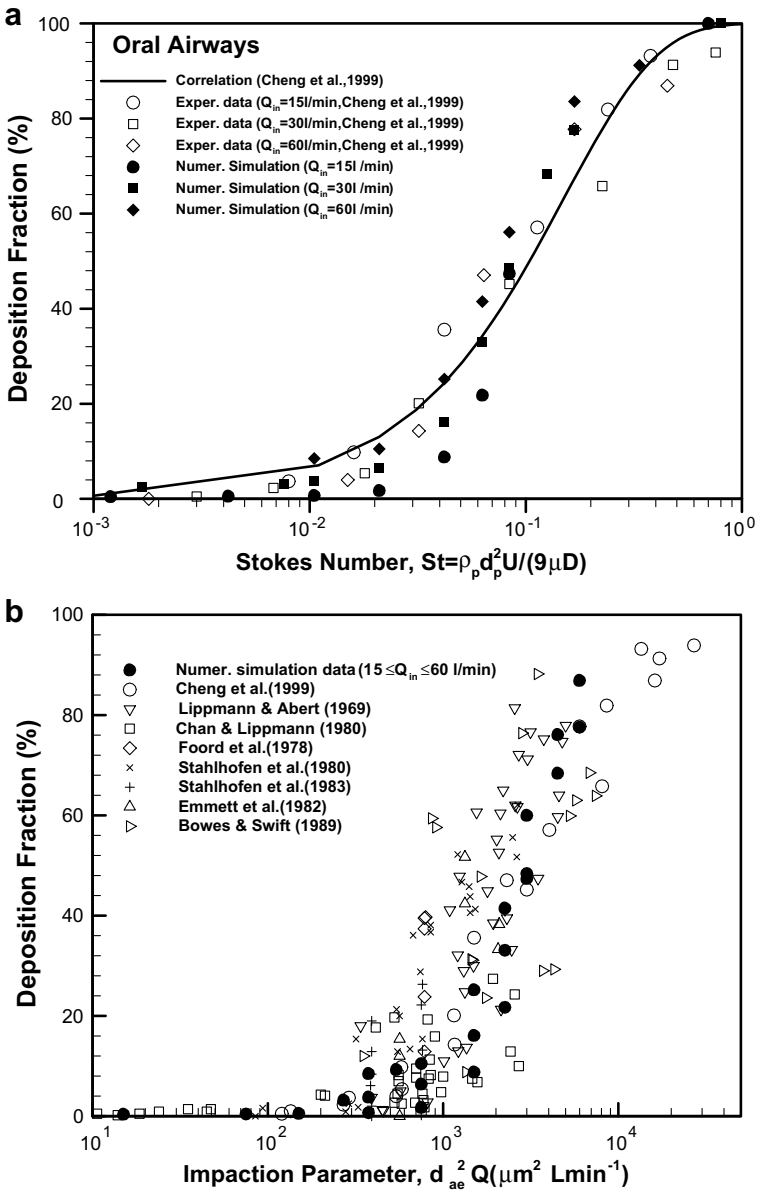

Fig. 2. Comparison of the present simulated particle deposition fractions in the oral airway model with: (a) the experimental data of Cheng et al. [24]; and (b) *in vitro* and *in vivo* deposition data sets, where d_{ae} is the aerodynamic particle diameter.

(IP = 392 μm^2 L/min; see Eq. (1)). Most of the particles can enter the deeper lung regions. In general, particles released from the left and right side of the circular mouth entrance enter the left and right lungs, respectively. However, the inlet positions of particles leaving different branches of G3 vary irregularly due to secondary flow effects. If the targeted regions are located in the upper airways, larger-size particles (e.g., 20 μm) should be employed to enhance the deposition with the present inhalation flow rate (i.e., 8 L/min).

Fig. 3c shows mouth inlet release positions of 7 μm particles which all reach eight outlets of Generation 3 in the *asymmetric* airway bifurcation model (see Fig. 1) when Q_{in} = 8 L/min. It is encouraging that the distributions of particle release positions look somewhat similar for targeting the outlets of two completely different tracheobronchial airway models. Specifically, the particle release regions which reach outlets of two sets of geometries with the same number (e.g., G3.8) are located at the same location or a neighboring site.

2.2. Experimental studies

An experimental proof-of-concept for the methodology of targeted aerosol delivery and comparisons with computational results have been conducted as well. Sodium chloride particles, with a mean particle size of about one micrometer were used to represent a drug aerosol in the laboratory experiments. The oral and symmetric four-generation (G0 to G3) bronchial airways were constructed out of laser-cured resin, using a three-dimensional solid printing method. The oral airway model has the same geometry as the computational model given in Fig. 1a and the symmetric four-generation bifurcation model is the same as shown in Fig. 1b. The particle distributions in the airways with different inlet release positions were recorded by a CCD camera. The experimental system mainly consists of a 3.81 centimeter PVC pipe, an aerosol generator, an oral airway model test section, an argon–ion laser and a Cohu CCD camera.

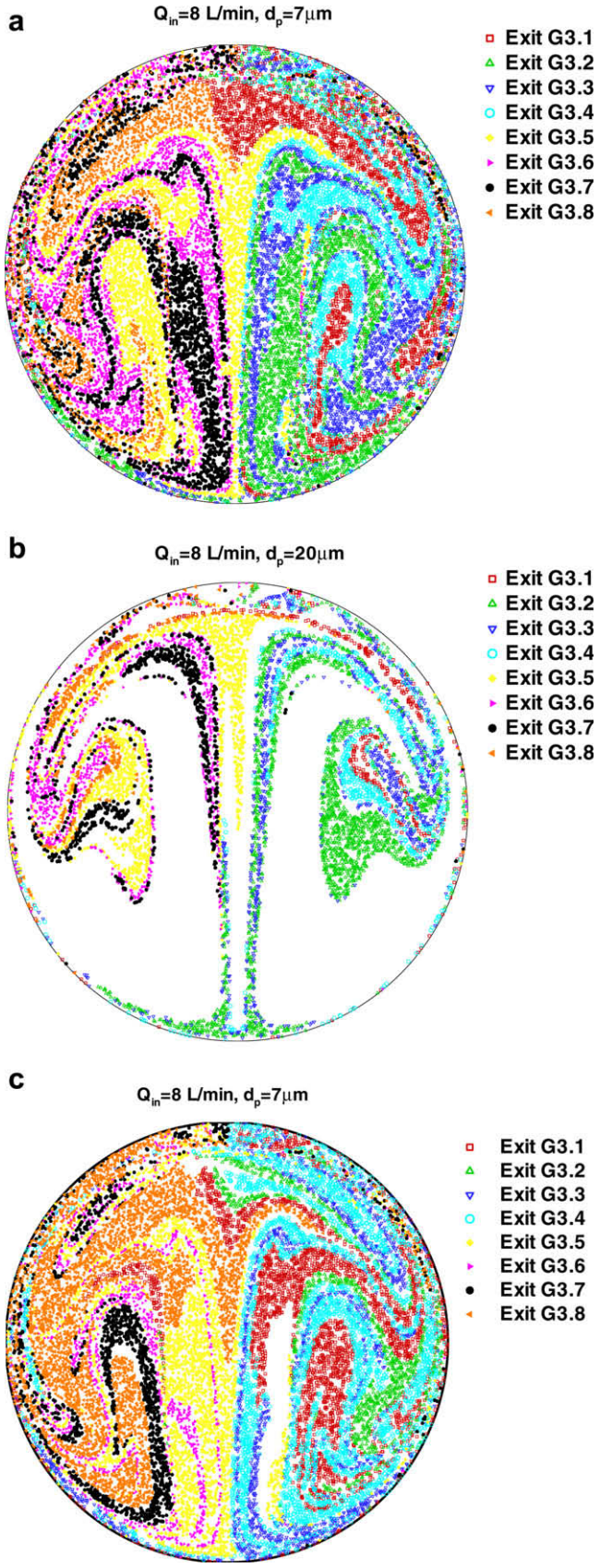

Fig. 3. Mouth inlet release positions of particles which land on or leave the upper airway model with: (a) symmetric, triple bifurcation model at Q_{in} = 8 L/min and d_p = 7 μm; (b) symmetric, triple bifurcation model at Q_{in} = 8 L/min and d_p = 20 μm; and (c) asymmetric, triple bifurcation model at Q_{in} = 8 L/min and d_p = 7 μm.

The transition of flow delivery from the PVC tube to the oral airway model was controlled by an inlet nozzle. This nozzle allows for the two separate flows to enter the test section in the correct orientation and location. The nozzle with a stationary seed tube was constructed again using a 3-D printing method. The seed tube exit with a 1 mm opening is offset from the centerline of the axisymmetric nozzle by 40% of the radius. Rotating the nozzle allowed the injection position to change. Fig. 4 shows the mouth of the oral airway labeled with injection angles for the experiments. A circle is drawn indicating the 40% radius location.

The aerosol generator used for this set of experiments was a Collison nebulizer. The base material used was a solution of sodium chloride (NaCl) and uranine dye (fluorescein) in water. The NaCl provided the majority of the particle volume; however, the uranine dye was essential for data acquisition. The use of a 3.7% NaCl aqueous solution allowed the generation of 1 μm particles. The TSI Incorporated Aerosol Particle Sizer Model 3310 (APS 3310) at the US EPA-HSD was used to measure the particles being generated by the nebulizer. Table 1 shows the measured data, including an unexpected low geometric standard deviation considering Collision nebulizers (Fig. 5); however, a slight deviation from the expected 1 μm particle size occurred.

The resin airway models that were made for testing were equipped with filter attachments. The filter attachments were designed to hold membrane filters cut with standard size grommet punches. In this study, the filters have a pore size of 1.2 μm and are able to capture particles smaller than 1.2 μm. An argon–ion laser emitting light at 488 nm was used to excite the fluorescent dye on each filter, which was placed in front of the laser beam at a 45° angle. The uranine dye has an excitation wavelength of 460 nm and

Fig. 4. Injection angles and 40% radius circle for oral airway experiments, looking into the mouth of the oral airway.

Table 1
Statistical data for 3.7% solution

	Particle diameter based on number	Particle diameter based on surface area	Particle diameter based on mass
Median (μm)[a]	0.848	0.956	1.07
Mean (μm)	0.924	1.10	1.26
Geometric mean (μm)	0.898	1.04	1.17
Mode (μm)	0.777	0.777	0.777
Geometric standard deviation (GSD)	1.25	1.37	1.44
Total concentration	106.8 (#/cm^3)	308.0 (μm^2/cm^3)	0.0565 (mg/m^3)

[a] The definition of median, mean, geometric mean and mode diameters as well as GSD can be found in Ref. [1].

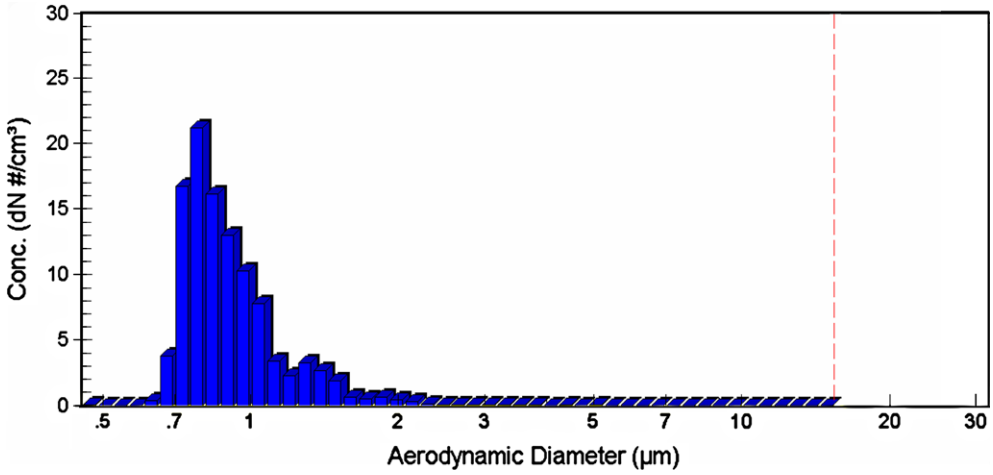

Fig. 5. Particle sizing results for 3.7% solution.

an emission wavelength of 515 nm. A Cohu CCD camera was positioned to collect the fluorescence photons directly off of the membrane filter. Two optical filters (to attain to the 488 nm scatter) were placed between the test filter and the camera lens for better imaging.

3. Results and discussion

3.1. Comparisons between computational and experimental results

The comparisons between the simulated and measured particle distributions with different inlet release positions for the oral airway model are shown in Fig. 6, assuming a steady inspiratory flow rate of 2 L/min. In simulations, 2000 spherical particles with a diameter of 1 μm were released at the mouth inlet. Clearly, the simulated particle distributions essentially agree with the experimental visualizations. The measured particles seem to be more dispersed when compared to the simulation results. This may be attributed to: (i) the droplets used for experiments are slightly polydispersed with a mean particle size of about 0.9 μm (see Table 1 and Fig. 5); (ii) droplet vaporization may occur during test, which my reduce the droplet size and affect the droplet trajectory [25]; and (iii) the effects of Brownian diffusion may become significant for small size particles (say, with $d_p < 1$ μm) so that the measured particle distributions are more dispersed. It also should be noted that the measured images cannot show the concentrations of particle distributions. Considering the common size range of inhaled drug aerosols is $d_p = 5$–20 μm, larger solid particles will be used at elevate flow rates in the future experimental studies. The following computational analyses will focus on particles with $d_p = 7$ μm again.

3.2. Particle release points on orbits with critical radii

As shown in Section 2.1.4, particles released from different fixed points, as can be achieved with a controlled nozzle, may enter different parts of the lower airways, i.e., after G3 (see Fig. 3). However, to set different drug-aerosol release nozzles universally at an inhaler outlet may pose challenges in manufacturing and operating a smart inhaler system for different patients and their diseases. Alternatively, for specific target areas, particles could be released from orbital points, as first indicated by Kleinstreuer et al. [3]. In this case, a tube-aligned nozzle with adjustable outlet diameter rotates following an orbit with critical radius (see Fig. 7). The nozzle can be positioned at a specific angle (or orbit location) so that most of the released particles can reach the desired lung section. For example, the targeted regions for release positions 1 and 2 shown in Fig. 7 are located in the lower airways after generation G3 of the symmetric airway model (i.e., the outlets of generations G3.1 and G3.8). Particles leaving from G3.1 enter the peripheral part of the left lung, while they transport into the outer portion of the right lung after exiting from G3.8 (see Fig. 1). Clearly, with the controlled inlets, the capture efficiency of particles in the targeted areas can increase from about 10% (normal inhalation) to almost 100% (controlled air-particle stream). Distributions of particles entering targeted (outlet) airways are depicted in Fig. 7 as well. Some particle dispersion occurs for Inlet Position 2–4 because of the influence of secondary flows, which will be further discussed in Section 3.3. In contrast, Inlet Position 1 is located in a larger, more uniform particle release area (see Fig. 3a) reaching the G3.1-airway outlet.

Fig. 8 depicts the inlet release positions and corresponding particle distributions at the targeted regions which are located at the outlets of generations G3.1 and G3.8 of the asymmetric bifurcation airway model. Of interest is that the release position for targeting the outlet of generation G3.8 are the same as that in the case of the symmetric airway model (i.e., both are Position #2). Similarly, the capture efficiencies can be as high as 100%.

As mentioned, a specific disease, lung tumor location, and/or suitable treatment determine the desired lung target site or region. Some of these predetermined deposition areas can be actually reached as demonstrated in Figs. 7 and 8. Implementation in terms of a SIS prototype is in progress.

3.3. Air-particle transport dynamics

The inhaled microparticle motion in the human upper airways is driven by complicated airflow structures; thus, a detailed analysis of the one-way coupled air-particle transport is helpful to understand the different particle trajectories and distributions originating from controlled release positions (see Fig. 7). As an example, the following discussion focuses on the oral and subsequent symmetric (Weible Type A) bronchial airway models. Which specific airway geometry is being considered is rather immaterial (see Fig. 7 vs. Fig. 8) because the new methodology can be applied to any lung morphology.

3.3.1. Airflow fields

Fig. 9 depicts the airflow streamlines (left panel) and velocity fields in the oral airway model with an inspiratory flow rate of

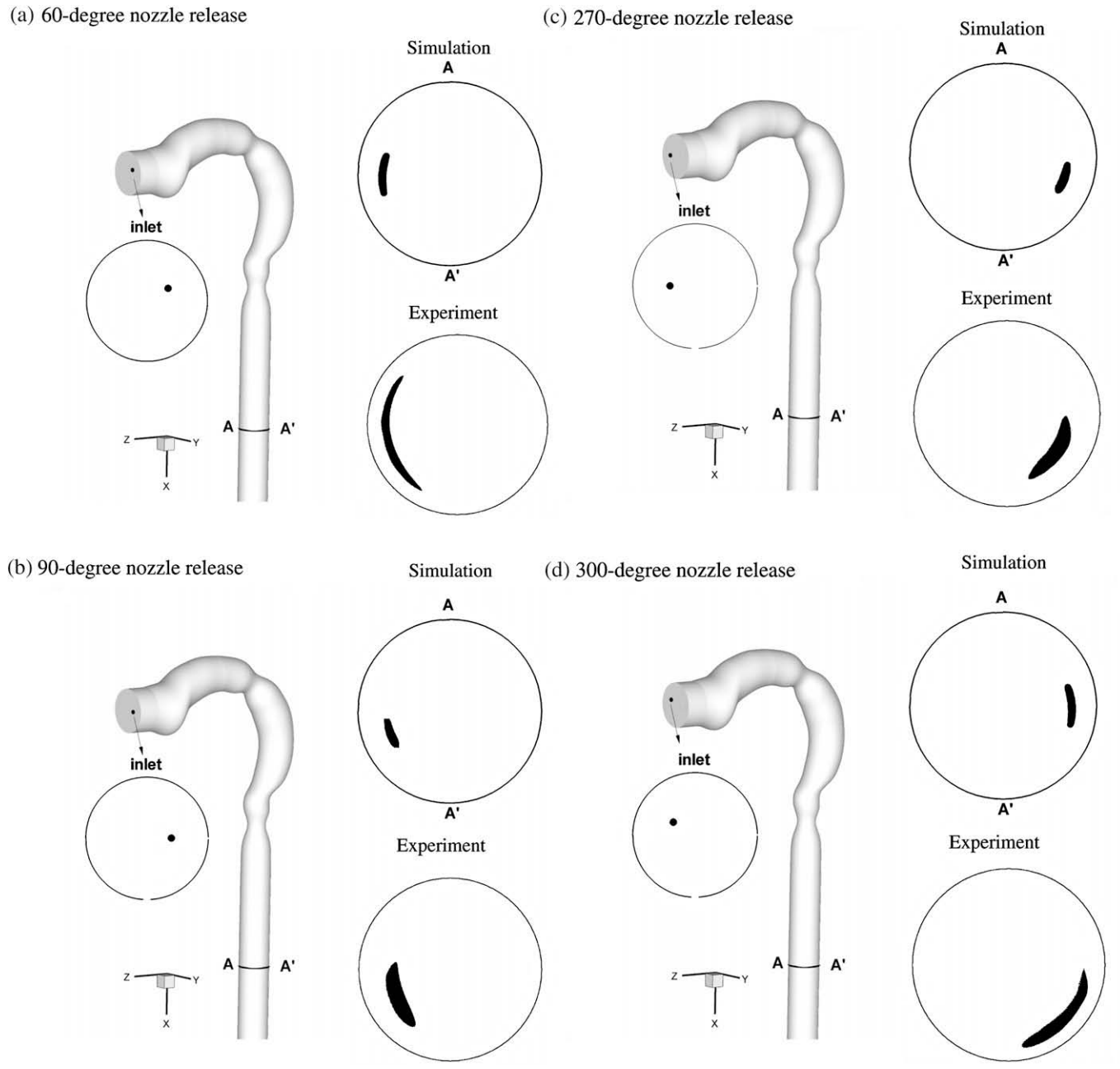

Fig. 6. Comparisons of simulated and measured particle distributions with different inlet release positions.

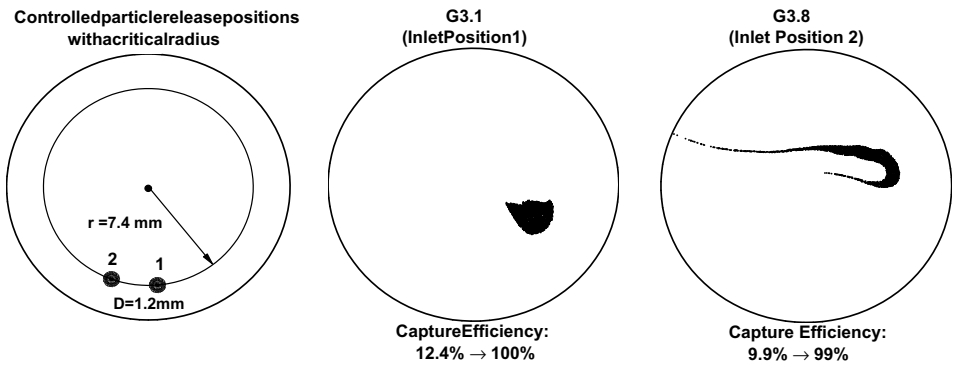

Fig. 7. Schematic of particles released with a critical radius and distributions of particles leaving different targeted tubes of generation G3 of the symmetric bifurcation airway model with different given release positions at the mouth inlet (Q_{in} = 8 L/min and d_p = 7 μm; dry air).

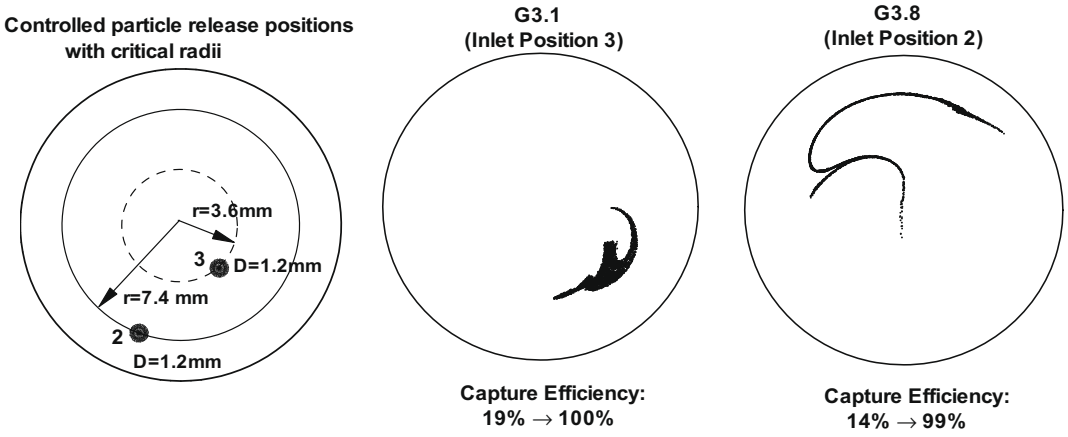

Fig. 8. Mouth inlet particle release positions and distributions of particles leaving different targeted tubes of generation G3 of the asymmetric bifurcation airway model with different given release positions at the mouth inlet (Q_{in} = 8 L/min and d_p = 7 μm; dry air).

Q_{in} = 8 L/min. The cross-sectional views display the axial velocity contours as well as secondary velocity vectors. The cross-sections C–C′, D–D′, E–E′ and F–F′ are zero, one, three, and six diameter(s) from the glottis, respectively. Clearly, the laminar airflow structures are quite similar to those at Q_{in} = 15 L/min which were discussed by Kleinstreuer and Zhang [22]. Specifically, the inhaled air velocity profiles are skewed to the outer bend due to the centrifugal force in the curved portion from the oral cavity to the pharynx/larynx, and then an asymmetric, central jet is created by the constriction of the vocal fold (glottis). Recirculating flows occur at regions with abrupt geometric changes, i.e., the variation of cross-sectional area in the lower portion of the mouth (near the tongue), the inside bend of the pharynx (Section B–B′), and downstream of the vocal fold. Secondary motion is set up when the flow

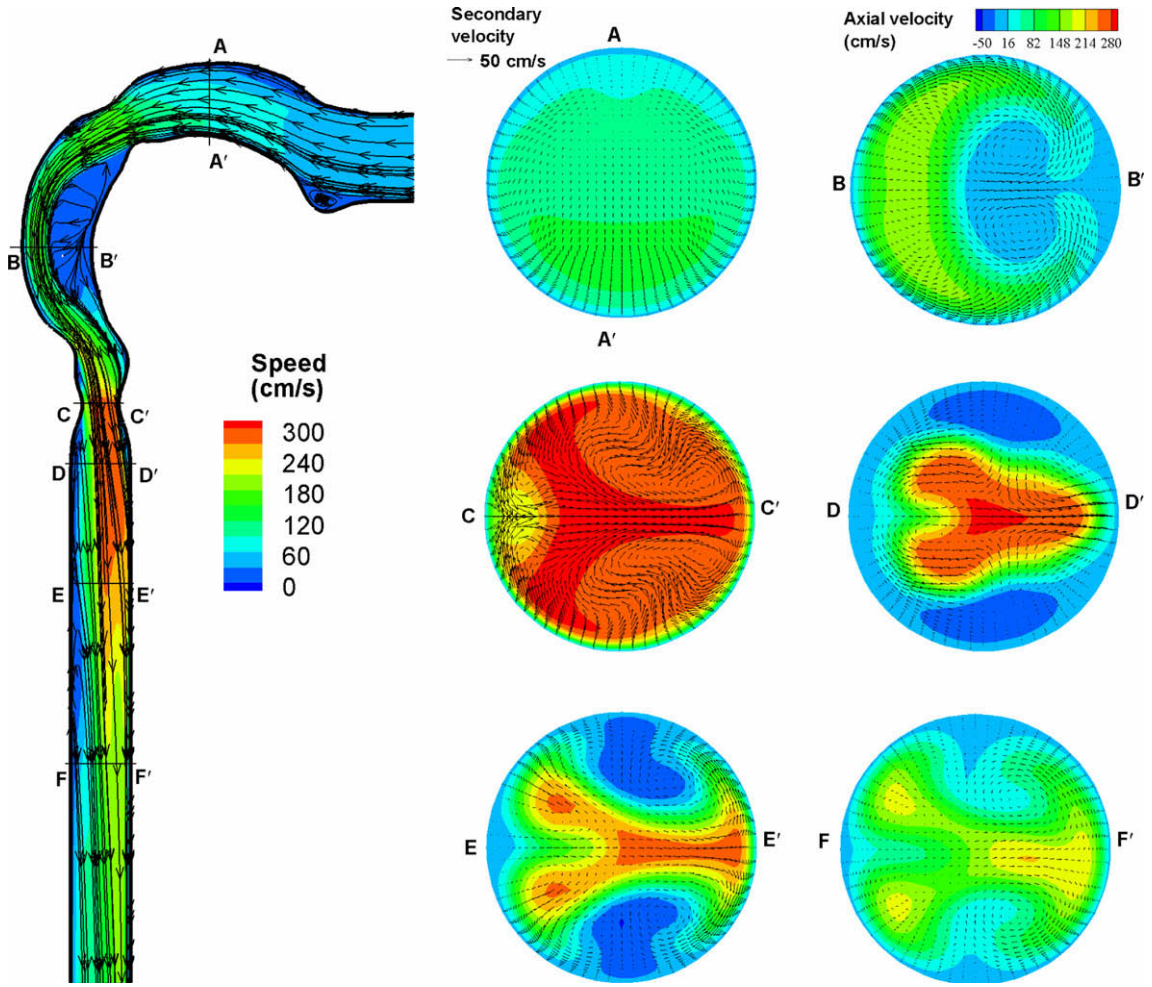

Fig. 9. Velocity profiles in the oral airway model at steady inhalation with Q_{in} = 8 L/min. The left panel exhibits mid-plane (y = 0 plane) airflow streamlines and speed contours. The right panel shows the axial velocity contours (magnitudes in cm/s) and secondary velocity vectors at different cross-sections.

turns a bend from the mouth to the pharynx because of the centrifugally induced pressure gradient. Secondary flows become more and more complicated downstream from the mouth when the air stream encounters an expansion or constriction with the variation of cross-sectional areas and continues to turn from the pharynx to the larynx. In addition, the interaction between secondary and axial motion also causes more complex flows, as indicated by the four distinct vortices observed at cross-section E–E′.

Fig. 10 shows the velocity fields in the symmetric, planar triple-bifurcation airways which are physiologically turned 90° with respect to the oral airways (see Fig. 1). Again, the selected cross-sectional views display the axial velocity contours as well as secondary velocity vectors. The inlet profiles for both axial and secondary velocities (see Section A–A′) are asymmetric about the bifurcation plane. Two zones with high axial velocities exist at the lower side of the tube (i.e., near the posterior wall of the trachea) while one high-velocity zone appears at the upper side of the tube (the anterior wall of the trachea). The air stream splits at the first flow divider and a new boundary layer is generated at the inner wall of the first daughter tube. The skewed profile with maximum axial velocities near the inner wall can be clearly observed at cross-sections B–B′ and E–E′. Another high-velocity region which appears near the upper side at section B–B′ may come from upstream. The locations and intensities of secondary vortices in the first daughter tube change as well, due to the centrifugal-force effects when compared to those at the parent tube (A–A′). When the air stream continues to turn through bends at the second and third daughter tubes, the velocity patterns vary with the development of upstream flows and the generation of the new boundary layers near the inner walls of the dividers. Of interest is that the entrance effects become relatively weak in the second and third daughter tubes. That is, the asymmetry of axial and secondary velocities about the bifurcation plane (i.e., mid-plane or $z = 0$ plane) is lower in the second and third daughter branches (see sections C–C′, D–D′, F–F′ and G–G′) than in the first daughter and parent tubes (B–B′, E–E′ and A–A′). Typical Dean flow can be observed in cross-sections D–D′ and G–G′. Specifically, two distinct secondary vortices occur at the upper and lower side of the tube, which moves the high-speed fluid up around the top of the tube towards the outside of the bifurcation and low-speed fluid from the outside of the bifurcation along the symmetry plane towards the inside of the bifurcation. The velocity fields at the left side of the triple bifurcation airway (see sections B–B′, C–C′, and D–D′) are quite similar to those at the right side (see sections E–E′, F–F′, and G–G′) due to the symmetry of the system geometry.

3.3.2. Microparticle transport

Cross-sectional particle distributions are useful to illustrate the impact of air flow structures, especially the effect of secondary flow on particle motion, and hence to elucidate basic physical insight. Particle trajectories and distributions at different cross-sections in the upper airway with the two controlled inlet release positions #1 and #2 (see Fig. 7) are shown in Figs. 11 and 12. The secondary velocity fields are also shown for easier interpretation of particle-stream dispersion.

Release position #1: Fig. 11a and b depict the particle trajectories and cross-sectional distributions in the oral and symmetric triple bifurcation airways, respectively. Particles are released from position #1 at the mouth inlet and the targeted site is the outlet of branch G3.1. Clearly, at the initial part of the oral airway (say, from the mouth inlet to section A–A′), the secondary velocities are very weak; hence, particles can follow the axial flow well and stay con-

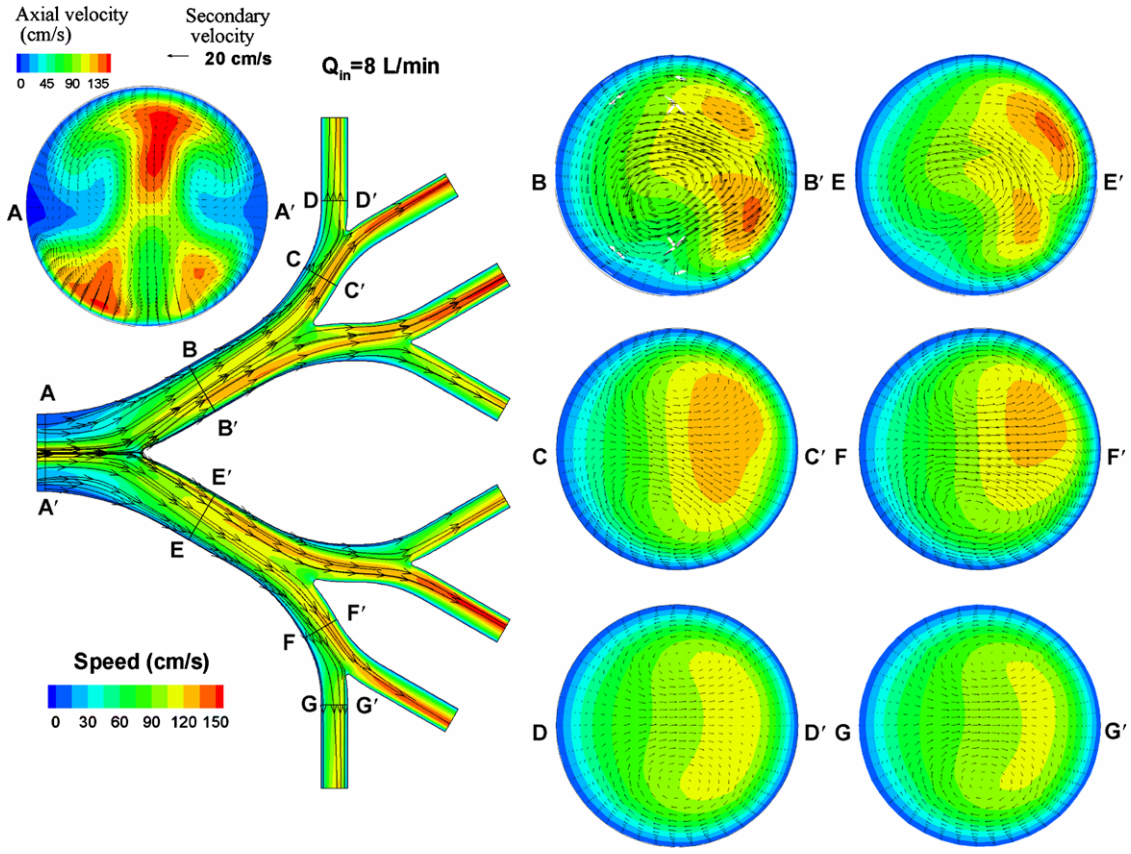

Fig. 10. Velocity profiles in the symmetric bifurcation airway model at steady inhalation with Q_{in} = 8 L/min. The left panel exhibits mid-plane ($z = 0$ plane) airflow streamlines and speed contours. The right panel shows the axial velocity contours (magnitudes in cm/s) and secondary velocity vectors at different cross-sections.

centrated. With the development of secondary flows in segment A–A′ to B–B′, both axial and secondary flows may affect particle transport. The particle stream moves from the lower, mid-plane location at section A–A′ to the left side of the tube at section B–B′ due to acceleration in the constriction of the soft palate, resulting in a skewed axial velocity profile and centrifugal force effect. Weak secondary flows may aid in the slight dispersion of the particle cluster. A strong, well-established secondary flow field may have a significant effect on the position and shape of the particle stream after the 180° bend at section B–B′. Specifically, in segment B–B′ to C–C′, vortical flow in cross-section B–B′ drives particles from the left to the upper and then right center of the airway (see C–C′). The non-uniform airflow fields "stretch" the particle cluster, i.e., some particles move faster in both planar and axial directions. In segment C–C′ to D–D′, the planar secondary flow will push particles from the center to the right side (see D–D′); then, the secondary

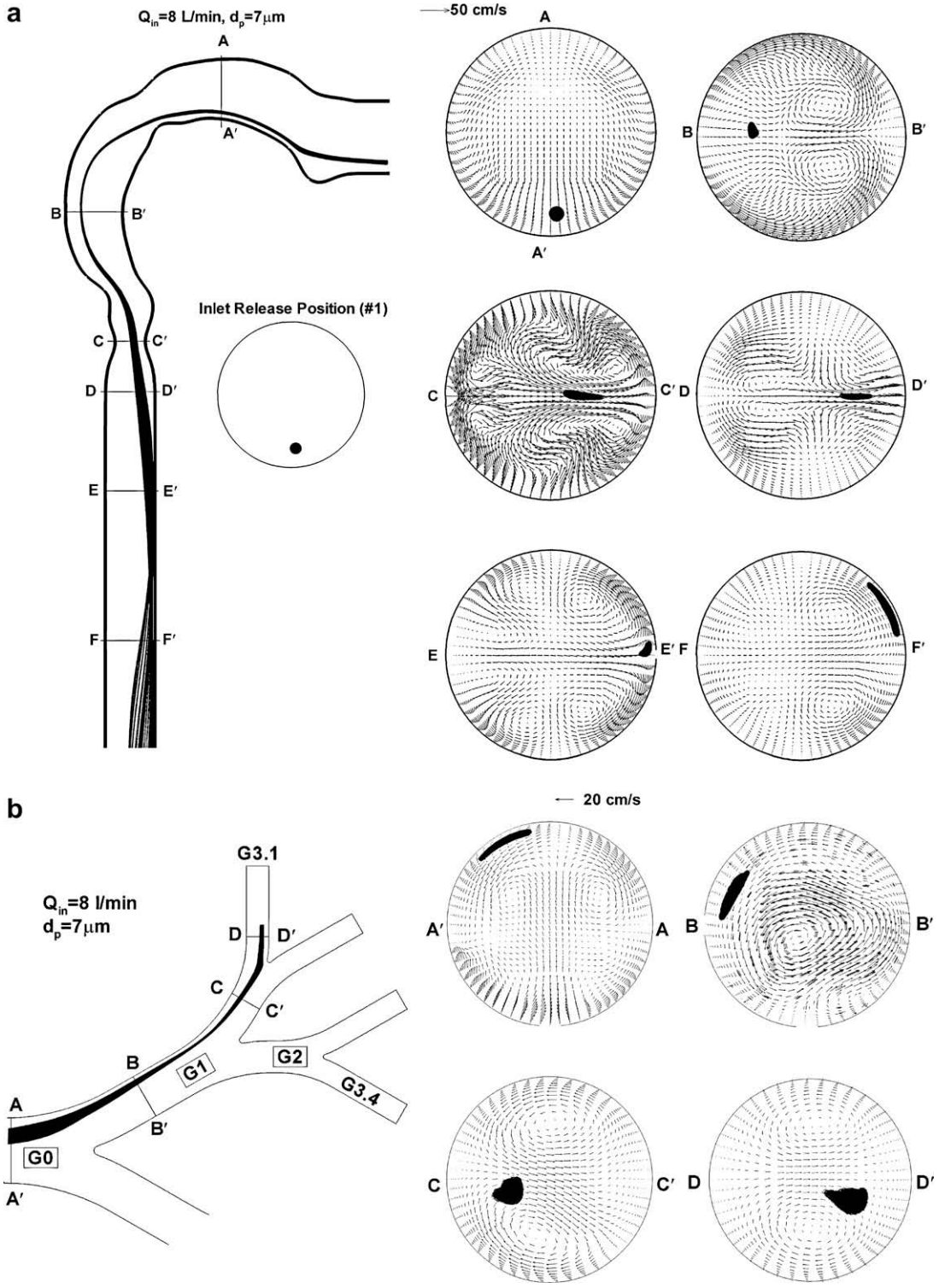

Fig. 11. Distributions of particles released from inlet position #1 with Q_{in} = 8 L/min and d_p = 7 μm at: (a) the oral airway model; and (b) the symmetric bifurcation airway model. The left panel exhibits the particle trajectories while the right panel depicts particle distributions and secondary velocity vectors at different cross-sections.

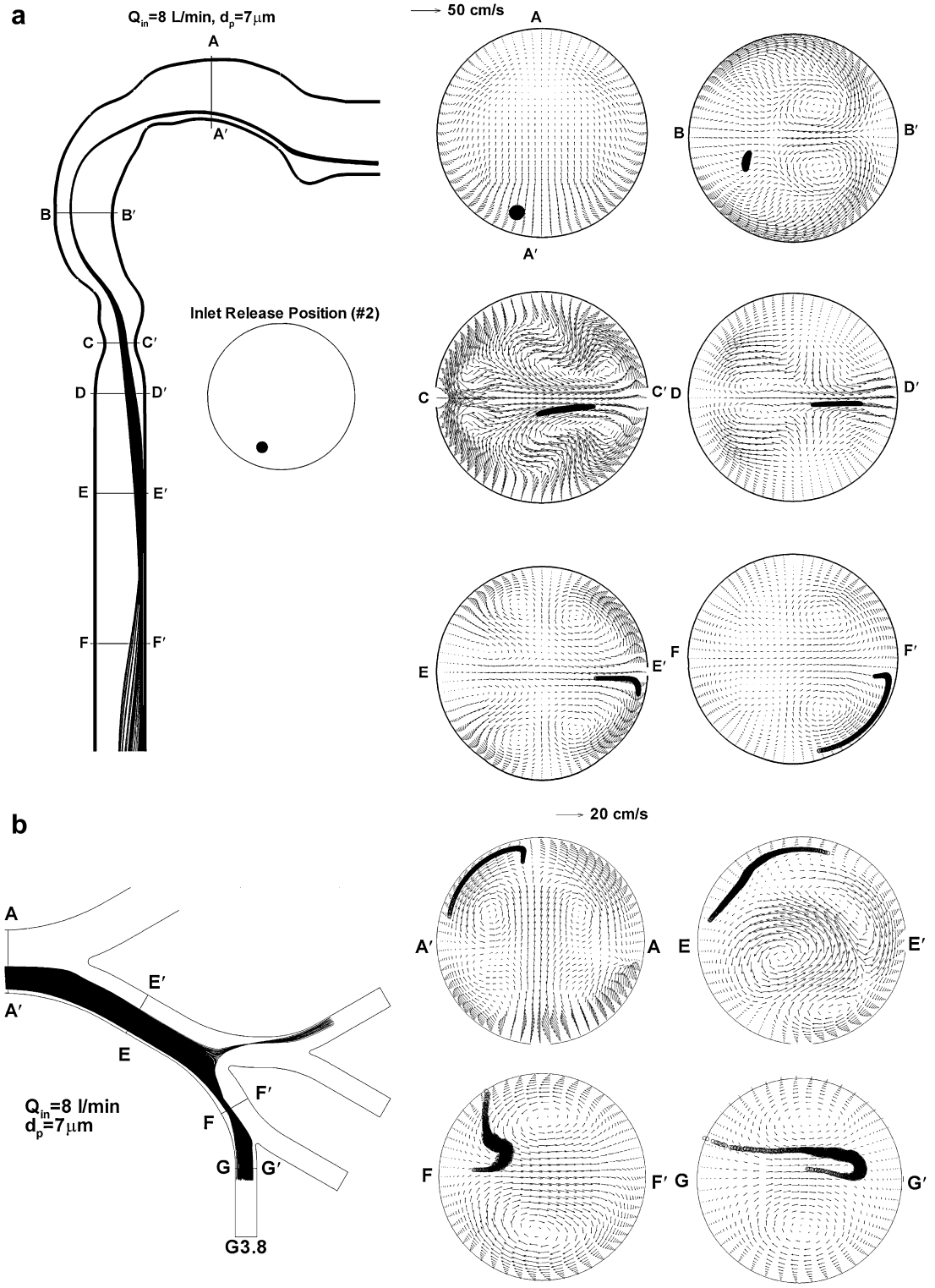

Fig. 12. Distributions of particles released from inlet position #2 with Q_{in} = 8 L/min and d_p = 7 μm at: (a) the oral airway model; and (b) the symmetric bifurcation airway model. The left panel exhibits the particle trajectories while the right panel depicts particle distributions and secondary velocity vectors at different cross-sections.

flow near the right wall of the tube may pull particles in the circumferential direction, generating a curved cross-section of the particle stream (see E–E′ and F–F′). The strong secondary flow behind the particle cluster results in the accumulation of particles in segment D–D′ to E–E′. However, the relatively large circumferential secondary flow near the right side of the airway wall will stretch the particle cluster again when traveling from E–E′ to F–F′.

The continuous variations in secondary flows occurring in the bifurcating airways induces further the lateral motion of the particle cluster (see Fig. 11b). The strong rotational airflow at the trachea exit (see A–A′) pushes particles toward the center of the G1 branch (see B–B′). It should be noted that the bifurcation airway is physiologically 90° turned with respect to the oral airways and the directional descriptions (i.e., left, right, upper, lower) used in the

discussion only refers to the relative positions shown in the cross-section of the Figs. 11 and 12, which are not related to the realistic physical positions. The downward secondary flows in generation G1 further pull particles towards the lower side of the tube. However, with the variation in secondary flows in the G2 (see C–C′), particles can be dragged up toward the tube center again. At the same time, the high-velocity secondary flow behind the particle cluster can aid in the concentration of particles as well. Finally, the particle cluster will be further pushed towards the right by the planar vortices encountered in generations G2 and G3 (see D–D′).

Release position #2: The entire situation for a particle cluster released from position #2 (see Fig. 7) with the outlet of G3.8 as the target is different because the particle stream (#2) encounters locally different secondary velocity fields (see Fig. 12). The movement of the particle stream #2 from the mouth inlet to section D–D′ in the oral airway model (see Fig. 12a) is similar to stream #1 (cf. Fig. 11a). When the stream cross-section is viewed in D–D′, it appears to be relatively long and a bit off the tube center when compared to cluster #1. Actually, cluster #2 is driven to the right lower portion of the branch airway, experiencing a more dispersed distribution. Correspondingly, cluster #2 enters a different side of the bronchial airway model (see Fig. 12b). Although cluster #2 can be somewhat "squeezed" by the relatively high secondary velocities pushing when it travels from sections E–E′ in G1 to F–F′ in G2, it may be further stretched by the local secondary flow fields due to its relatively long range. Finally, particles are quite dispersed at the outlet of generation G3.8 (see G–G′). Generally speaking, the particle cluster is easier to be stretched by secondary flows than to be squeezed. The secondary flow effects influencing the transport and dispersion of microparticles are the same for the *asymmetric* triple bifurcation airway model (Fig. 1c); hence, it will not be further discussed.

Although the present simulations assume dry air properties, the variations of density and dynamic viscosity of moist air encountered in the actual lung airways are within 1.2% when compared to dry air. However, the situation for hygroscopic aerosols, in terms of trajectories and planar dispersion, is different if considering the high humidity environment [25].

4. Conclusions

Both computational and experimental studies show that micron particles may follow tractable trajectories in human lung airways under steady laminar flow conditions. Hence, the specific mouth inlet (or inhaler inlet) positions of aerosols which enter different lung regions or land on different targeted lung sites can be determined via backtracking. With the optimal combination of particle size, particle release position and inhalation waveform, the delivery efficiency of inhaled drug aerosols to the desired areas may greatly improved. The dispersion (or stretching/squeezing) of released particles at different cross-sections of the airways is mainly driven by secondary flows.

Acknowledgements

The authors would like to thank Dr. C.S. Kim (Human Studies Division, U.S. EPA, RTP, NC) for providing instrumentation and laboratory space to conduct the reported experiments. Use of the particle-inlet nozzle, courtesy of Prof. S.T. Seelecke (MAE Dept., NCSU, Raleigh, NC), is acknowledge as well. This effort was sponsored by the NIH grant 8R21EB006717-02.

References

[1] W.H. Finlay, The Mechanics of Inhaled Pharmaceutical Aerosols: An Introduction, Academic Press, London, UK, 2001.
[2] P. Atkins, T. Crowder, A. Hickey, K. Johnson, S. Kraabel, D. Mckinney, Recent technical advances and formulation strategies in pulmonary drug delivery, Pharmaceut. Manufact. Pack. Sourcer (2003).
[3] C. Kleinstreuer, H. Shi, Z. Zhang, Computational Analyses of a Pressurized Metered Dose Inhaler and a New Drug-Aerosol Targeting Methodology, J. Aerosol Med. 20 (2007) 294–309.
[4] C.L. Leach, P.J. Davidson, R.J. Boudreau, Improved airway targeting with the CFC-free HFA-beclomethasone metered-dose inhaler compared with CFC-beclomethasone, Euro. Resp. J. 12 (1998) 1346–1353.
[5] Y.S. Cheng, C.S. Fu, D. Yazzie, Y. Zhou, Respiratory deposition patterns of salbutamol pMDI with CFC and HFA-134a formulations in a human airway replica, J. Aerosol Med-Deposit. Clear. Effects Lung 14 (2001) 255–266.
[6] C. Kleinstreuer, Z. Zhang, Targeted drug aerosol deposition analysis for a four-generation lung airway model with hemispherical tumors, J. Biomech. Eng. – Trans. ASME 125 (2003) 197–206.
[7] K.H. Cheng, Y.S. Cheng, H.C. Yeh, D.L. Swift, Measurements of airway dimensions and calculation of mass transfer characteristics of the human oral passage, J. Biomech. Eng. – Trans. ASME 119 (1997) 476–482.
[8] E.R. Weibel, Morphometry of the Human Lung, Academic Press, New York, 1963.
[9] Z. Li, C. Kleinstreuer, Z. Zhang, Simulation of airflow fields and microparticle deposition in realistic human lung airway models. Part I: Airflow patterns, Euro. J. Mech. – B/Fluids 26 (2007) 632–649.
[10] K. Horsfield, G. Dart, D.E. Olson, G.F. Filley, G. Cumming, Models of the human bronchial tree, J. Appl. Phys. 31 (1971).
[11] O.G. Raabe, H.C. Yeh, G.M. Schum, R.F. Phalen, Tracheobronchial Geometry: Human, Dog, Rat, Hamster, LF-53, Lovelace Foundation Report, Albuquerque, New Mexico, 1976.
[12] Y. Zhang, W.H. Finlay, Measurement of the effect of cartilaginous rings on particle deposition in a proximal lung bifurcation model, Aerosol Sci. Technol. 39 (2005) 394–399.
[13] Z. Zhang, C. Kleinstreuer, Transient airflow structures and particle transport in a sequentially branching lung airway model, Phys. Fluids 14 (2002) 862–880.
[14] C. Kleinstreuer, Biofluid Dynamics: Principles and Selected Applications, CRC Press, Boca Raton, FL, 2006.
[15] C. Kleinstreuer, Z. Zhang, C.S. Kim, Combined inertial and gravitational deposition of microparticles in small model airways of human respiratory system, J. Aerosol Sci. 38 (2007) 1047–1061.
[16] R. Clift, J.R. Grace, M.E. Weber, Bubbles, Drops, and Particles, Academic Press, NY, 1978.
[17] P.W. Longest, C. Kleinstreuer, J.R. Buchanan, Efficient computation of micro-particle dynamics including wall effects, Comput. Fluids 33 (2004) 577–601.
[18] Z. Zhang, C. Kleinstreuer, J.F. Donohue, C.S. Kim, Comparison of micro- and nano-size particle depositions in a human upper airway model, J. Aerosol Sci. 36 (2005) 211–233.
[19] J.K. Comer, C. Kleinstreuer, S. Hyun, C.S. Kim, Aerosol transport and deposition in sequentially bifurcating airways, J. Biomech. Eng. – Trans. ASME 122 (2000) 152–158.
[20] J.K. Comer, C. Kleinstreuer, Z. Zhang, Flow structures and particle deposition patterns in double-bifurcation airway models. Part 1. Air flow fields, J. Fluid Mech. 435 (2001) 25–54.
[21] Z. Zhang, C. Kleinstreuer, C.S. Kim, Gas-solid two-phase flow in a triple bifurcation lung airway model, Int. J. Multiphase Flow 28 (2002) 1021–1046.
[22] C. Kleinstreuer, Z. Zhang, Laminar-to-turbulent fluid-particle flows in a human airway model, Int. J. Multiphase Flow 29 (2003) 271–289.
[23] Z. Zhang, C. Kleinstreuer, Low-Reynolds-number turbulent flows in locally constricted conduits: A comparison study, AIAA J. 41 (2003) 831–840.
[24] Y.S. Cheng, Y. Zhou, B.T. Chen, Particle deposition in a cast of human oral airways, Aerosol Sci. Technol. 31 (1999) 286–300.
[25] Z. Zhang, C. Kleinstreuer, C.S. Kim, Water vapor transport and its effects on the deposition of hygroscopic droplets in a human upper airway model, Aerosol Sci. Technol. 40 (2006) 1–16.